Experimental Investigation into the Air Compressibility Scaling Effect on OWC Performance and Wave Height

Nadav Cohen, Francois Flocard, Ian L. Turner, Nataliia Sergiienko, Ben Cazzolato.

Abstract—**Wave energy converter arrays have the potential to provide coastal protection in addition to generating power from incoming waves. As part of a wider experimental study to investigate dual-use applications, this paper presents the results of wave flume testing conducted to analyse the performance characteristics of a single, generic Oscillating Water Column (OWC) device, in preparation for the next phase of study that will focus on multi-device arrays. The specific focus of this flume testing was to characterise parameters such as Response Amplitude Operator (RAO), Capture Width Ratio (CWR) and Phase Response, as well as the device's effect on the local wave field.**

A potential limitation when using scaled experimental results for OWCs are the differing scaling factors that should be applied to the device's submerged volume (λ^3) and air volume (λ^2) which, together with the Power Take Off (PTO) damping, can greatly affect the air-spring stiffness experienced within the OWC.

A subset of 34 tests (out of a total 134) were conducted under monochromatic wave conditions with wave heights of 20 mm or 40 mm and wave periods ranging from 1.2 s to 2.2 s. In these tests the PTO damping was varied by adjusting the orifice diameter, while the air volume was varied via an adjustable auxiliary air chamber. Results show that for the smaller orifice diameters (i.e., higher damping) tested, air-spring stiffness played a significant role and counterintuitively increased with increased air volume.

Effects of the single OWC device on the wave field within the flume were also investigated. Results revealed that while there is a marked difference when comparing the OWC to an identically-shaped blockage, there was no significant measurable difference in the wave height change observed for all the damping and air volume parameter settings that were modelled, despite a general trend when comparing to the empty flume.

This research is funded by the Australian Government through the Australian Research Council (project number LP180101109).

N.C., I.T., F.F. Authors are affiliated with the Water Research Laboratory, School of Civil & Environmental Engineering, UNSW Sydney, NSW, 2093, Australia (e-mail: nadav.cohen@unsw.edu.au).

N.S and B.C. Authors are affiliated with the University of Adelaide, SA, 5005, Australia (e-mail: nataliia.sergiienko@adelaide.edu.au).

Digital Object Identifier: https://doi.org/10.36688/ewtec-2023-242

Keywords—**Oscillating Water Column, Scaling, Compressibility, Experiments, Response Amplitude Operator, Phase Response, Capture Width Ratio.**

I. INTRODUCTION

IN order for wave energy converter (WEC) technologies to potentially reach the higher levels of technological maturity that other renewable energy generation sources have achieved, synergistic or niche applications unique to wave energy should be explored [1]. Among WECs, the Oscillating Water Column (OWC) has been widely studied and modelled (both physically and numerically) as well as a growing number of full-scale devices deployed [2], and can be considered as one of the more mature WEC technologies at the current time.

Model scale testing continues to play an important role in the development and advancement of ocean renewable energy technologies, serving as a critical step in validating and assessing the viability of these devices [3]. A wide range of deployment strategies for OWC-type devices have been proposed and include isolated, breakwater integrated and arrays. Investigations have focused primarily on improving the hydrodynamic performance and overall power of the device or array [4-16].

An important limitation in modelling OWCs highlighted in [17] arises when using scaled experimental results for OWCs. This occurs because Froude scaling is generally employed in the laboratory, as gravitational and inertial forces tend to be the dominant factors within the device hydrodynamics. However, the air compressibility cannot be effectively scaled using this criterion, which can then lead to misleading predictions of full sized device performance [12]. As a result it has been suggested that scaling the air chamber volume by the length scale squared (λ^2) rather than the Froude volumetric scaling (λ^3) may be more appropriate [17]. A number of studies, e.g. [8, 9, 18-21] have addressed this issue by attaching additional auxiliary air tanks to the air chamber of a single device to allow for appropriate air compression to occur.

Constructing an array of multiple OWCs for use in wave basin experiments, each with its own large air chamber, is generally not feasible nor practical. As a

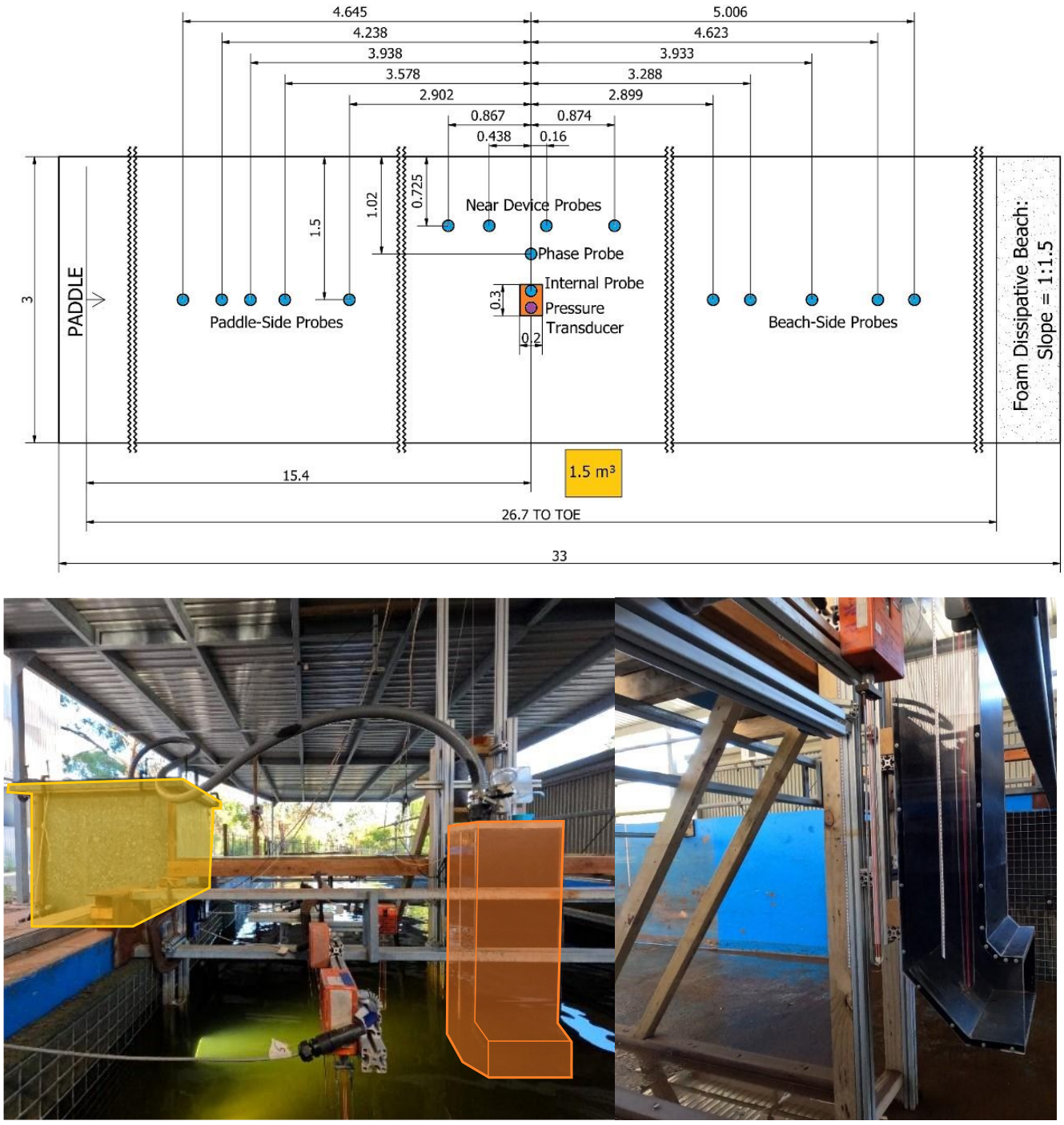

Fig. 1. Plan View of Experiment (Top); Experimental Setup showing OWC and Air Chamber (Bottom-Left); Empty Flume with OWC and rigid wooden frame (Bottom-Right)

result, a common approach is to ignore these potential air compressibility scaling effects. Additionally, when testing 'generic' devices of an indeterminate scale, it is unclear how to address the air compressibility issue.

This paper presents the results of wave flume testing (Fig. 1) carried out to characterise a single, 'generic' OWC device, in preparation for multiple device array testing in a wave basin at a later stage. The primary focus of the future basin study is to explore the use of OWC arrays for coastal protection. As such, in assessing the performance of the device tested, effects on the wave field will be explored in addition to the Response Amplitude Operator (RAO), Capture Width Ratio (CWR) and Phase response.

II. Experimental Design

A. OWC Geometry

So that the results of this study can be applied to OWCs in general as opposed to a specific commercial design, a generic, bent duct OWC geometry with a rectangular cross section was chosen. To simplify the hydrodynamics for future array studies, this paper focusses on offshore-stationary OWCs, a configuration previously studied as a single bent duct OWC by [12, 22-24] and as both a single and array cylindrical OWC by [13, 25]. The device was constructed from 18 mm plywood with a 200 mm x 300 mm cross section (Fig 2). It

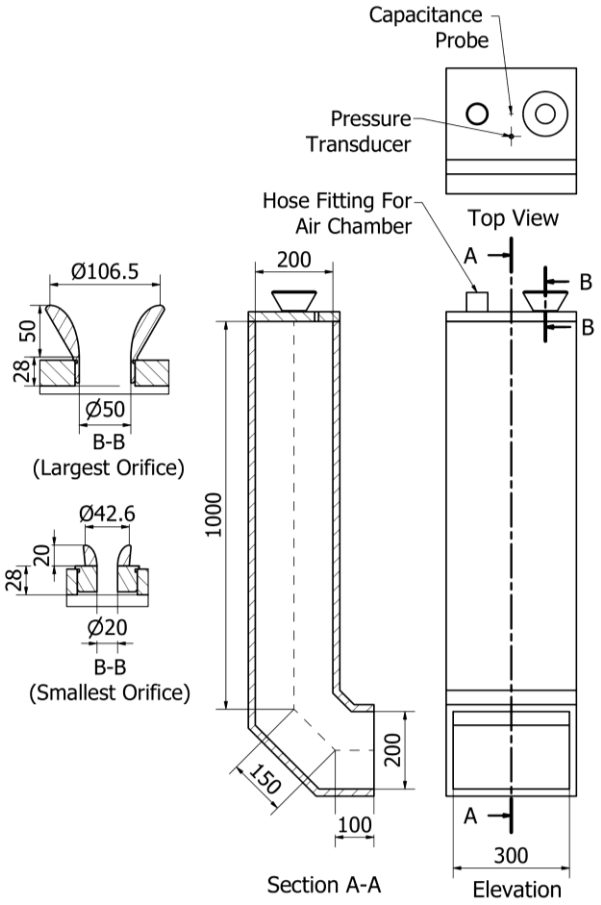

Fig. 2. Dimensioned OWC Design with largest and smallest orifice size on left

was rigidly mounted on a wooden frame attached to the flume floor. All comparative flume tests without the device were conducted with the frame in place to include any wave field effects (however small) from the frame.

B. *Air Chamber Design*

An air chamber with an adjustable volume up to 1.5 m³ was attached via a 50 mm diameter vacuum hose, 4.6 m in length and situated in parallel to the orifice (Fig. 1). The air chamber hose port on top of the OWC (Fig. 2) could be blocked completely to perform tests without the chamber. The air chamber volume was adjusted by partially filling it with water.

C. *Power Take Off*

To simulate the Power Take Off (PTO) a bell-mouth funnel orifice was attached to the top plate. Seven diameters of orifices (20 mm to 50 mm in 5 mm increments) were tested to allow for adjustability in PTO damping (smallest and largest shown in Fig. 2). Additional tests were performed with no top plate, and with the submerged entrance blocked (labelled 'Open' and 'Blocked' in subsequent figures). The bell-mouth funnel shape was chosen to reduce an aeroacoustic resonance phenomenon observed in the pressure signal during preliminary testing (see Fig. 3). This phenomenon, referred to as Helmholtz resonance, was caused by the initial sharp-edged design of the orifice plates creating flow instabilities. This resonance occurred on the inhale only and resulted in a pressure fluctuation greater than the pressure signal from the excitation of the free surface.

Changing the design of the orifice plate to a bell shape design with thicker orifice walls allowed for lower instabilities and so did not trigger the Helmholtz resonance.

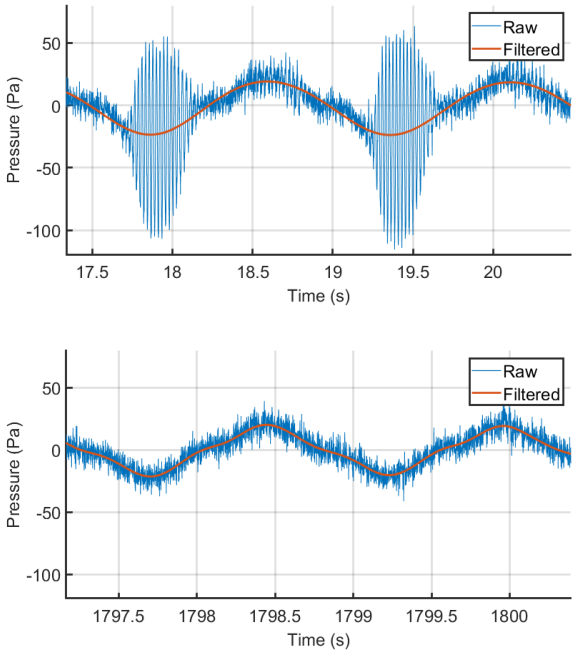

Fig. 3. Aeroacoustic resonance in preliminary as a result of a sharp orifice entrance (top). Similar conditions but orifice replaced with bell-mouth funnel (bottom)

D. *OWC Instruments*

The OWC device was fitted with a capacitance wave probe, measuring the amplitude response of the internal free surface with a precision of ±1 mm. An Omega PXM409-350HDWUUSBH differential pressure transducer was used to measure the air pressure difference between the internal OWC air pressure and atmospheric pressure. A recording artifact was observed between the pressure and wave probe time series which had to be corrected during post-processing. This resulted in an inherent reduction in the accuracy of the CWR analysis.

TABLE I
WAVE CONDITIONS PRESENTED

Wave Condition	Height (mm)	Number of Waves	Periods (s)										
Monochromatic	40	20 (per period)	1.2	1.3	1.4	1.5	1.6	1.7	1.8	1.9	2.0	2.1	2.2
	20					1.53	1.63	1.73	1.83				
						1.55	1.65	1.75	1.85				
						1.57	1.67	1.77	1.87				

TABLE II
TESTING MATRIX PRESENTED

Chord Length (mm)	Orifice Diameter (mm)	Additional Air Volume (L)			
N/A	No Device	N/A			
565	20	0			
	25	0	594	1064	1538
	30	0			
	35	0	594	1064	1538
	40	0			
	45	0	594	1064	1538
	50	0			
	Open	0			

E. Test Facility

Physical model testing was conducted at the UNSW Water Research Laboratory in a 3 m wide by 32.5 m long wave flume set with a constant water depth of 1 m. Capacitance wave probes with a precision of ±1 mm were placed in 3 groups of 5 probes as shown in Fig. 1 to measure the wave field in front, behind and adjacent to the OWC. One of the 'near device' probe locations (referred to as the 'Phase Probe') was aligned with the centerline of the OWC in order to measure the phase delay between the incident wave and the free surface excitation.

A foam dissipative beach at the end of the flume was used to attenuate reflected waves.

F. Device Configurations and Test Conditions

Several OWC parameters, including device draft, orifice diameter and air chamber volume, were varied throughout an extensive testing program. In total, 44 different device configurations were tested with regular waves, and a limited subset of configurations were tested using an irregular JONSWAP wave condition as well as a chirp signal which is a sweep of wave frequencies from long to short waves [26]. In all, 135 runs were conducted. This paper presents the results from the regular (monochromatic) wave periods at a single draft (L_c = 565 mm) varying the orifice diameter and air chamber volume. In total 17 configurations tested at 2 wave heights totalling 34 runs tested with 23 monochromatic periods per run. The wave conditions presented in this paper are summarised in Table I and the testing matrix in Table II.

III. ANALYSIS AND RESULTS

The focus of this flume testing campaign was to characterise parameters such as RAO, CWR and Phase Response, as well as the potential effect of the device on the wave field around the device.

G. Response Amplitude Operator

The Response Amplitude Operator (RAO) refers to the transfer function of a device to the prevailing sea state. Experimentally this is determined by:

$$RAO = \frac{H_{owc}}{H_w} \tag{1}$$

where H_{OWC} is the mean wave height of the internal free surface within the device and H_w is the mean wave height of the incident waves. Experimentally, the number of waves used for each monochromatic period was based on the time it took for the first reflection from the beach to reach the device. The H_w was found using the mean wave height of the 'Near Device Probes' indicated in Fig. 1. The experimentally derived RAOs were further compared to the solution to the equations of motion for a linear oscillator in the frequency domain, [27-29] which can be expressed as:

$$M_w\ddot{x} = F_e + F_{hs} + F_{rad} + F_{vis} + F_P \tag{2}$$

where $\ddot{x}$ is the vertical acceleration of the free surface, F_e is the excitation force, F_{hs} is the force from the hydrostatic pressure, F_{rad} are the radiation forces, F_{vis} are the forces from viscous losses, F_P is the force damping the free surface oscillation due to air pressure generated by change of the internal air volume.

Under linear conditions, the equations of motions can be expressed as:

$$M\ddot{x} + C\dot{x} + Kx = F_e \tag{3}$$

where $M\ddot{x}$ represents inertial forces, Kx the restoring forces and C representing losses in the system.

Or, in terms of damping ratio and resonant frequency

$$\ddot{x} + 2\zeta\omega_0\dot{x} + \omega_0^2 x = \frac{F_e}{M} \tag{4}$$

where the resonant angular frequency $\omega_0 = \sqrt{\frac{K}{M}}$ and the damping ratio $\zeta = \frac{C}{2M\omega_0}$.

The inertial forces can be decomposed into the mass of water in the system and the frequency dependent added mass (M_a), which is assumed constant. M_a is a measure of the inertial interaction with the surrounding fluid and is a component of F_{rad}. The total effective mass M is given by:

$$M = M_w + M_a = \rho_w A_w L_c + M_a \tag{5}$$

where ρ_w is the water density, A_w is the cross-sectional area of the OWC and L_c is the chord length of the water column.

F_{rad}, F_{vis} and F_P contribute to the losses in the system (C) and are taken a single constant incorporated in ζ.

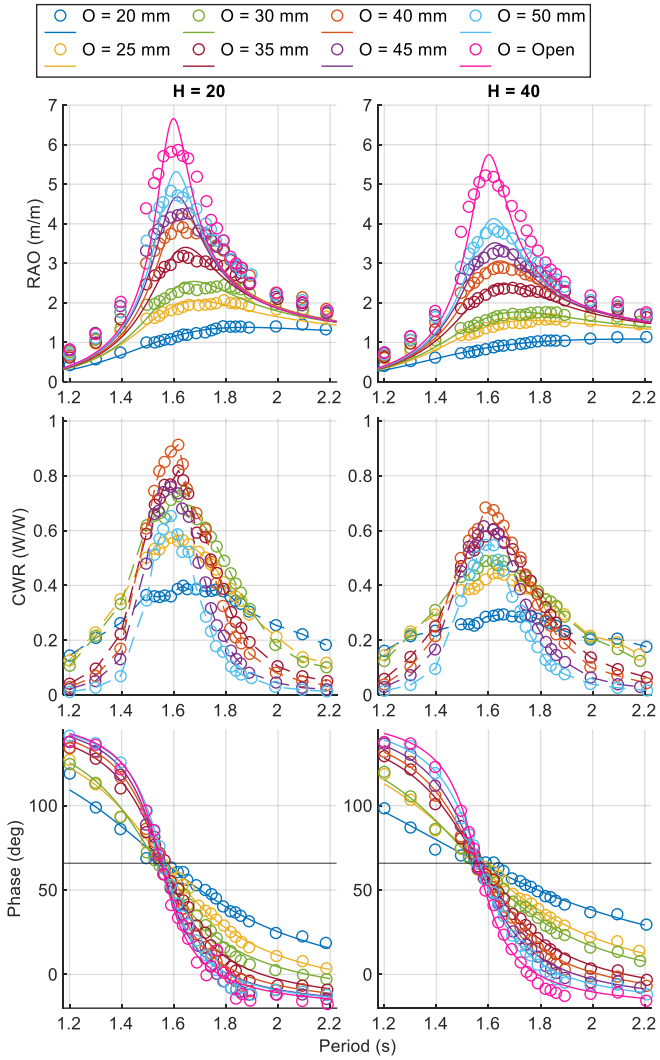

Fig. 4. Performance characteristic for all orifice diameters (O = [20, 25, 30, 35, 40, 45, 50] mm and Open) with no added air chamber (AC = 0). RAO (top) and Phase (bottom) results compare experimental results (circles) and the numerical fit (solid lines). CWR (middle) show experimental results only.

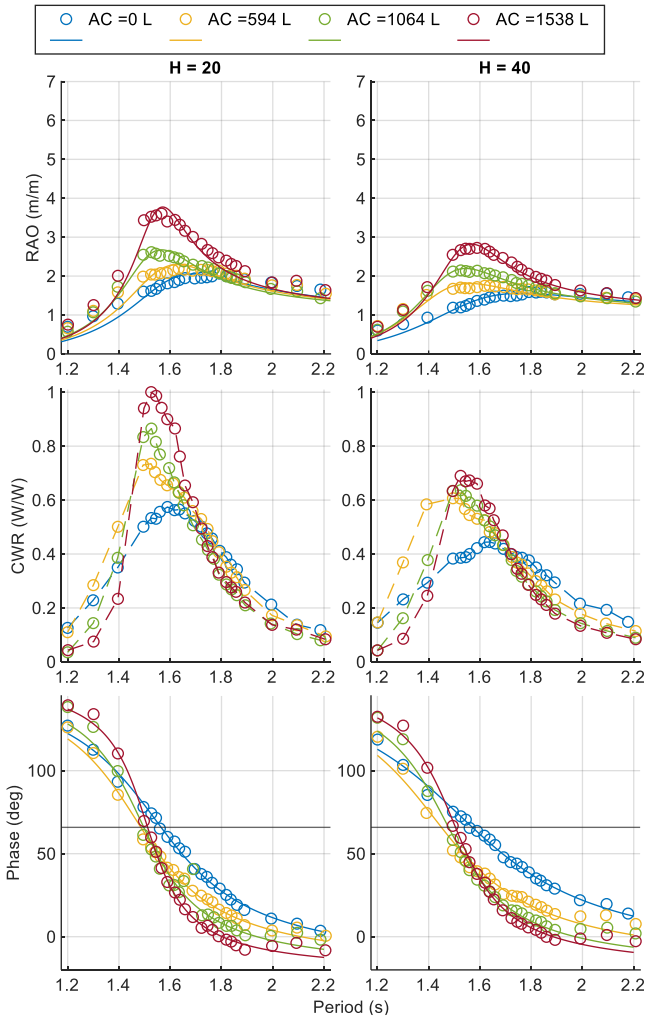

Fig. 5. Performance characteristic for single orifice diameter O = 25 mm added air chamber (AC = [0, 594, 1064, 1538] L). RAO (top) and Phase (bottom) results compare experimental results (circles) and the numerical fit (solid lines). CWR (middle) show experimental results only.

The restoring forces include the hydrostatic force (F_{hs}) expressed in equation (6) and the air-spring stiffness associated with the radiation susceptance of the volume flow which is a component of F_P [30]

$$K = K_{hs} = \rho_w A_w g \tag{6}$$

F_e is the excitation force exerted on the submerged entrance from the dynamic pressure (p_{dyn}) of the incident wave. According to linear wave theory this is given as [28, 29]

$$F_e = p_{dyn} \cdot A_w \tag{7}$$

$$p_{dyn} = \frac{\rho_w g H_w}{2} \cdot \frac{\cosh\big(k(d - L_e)\big)}{\cosh(kd)} \cdot \sin(\omega t) \tag{8}$$

where k is the wave number, d is the total depth of the water column in the vicinity of the device and L_e is the entrance depth taken as the depth of the midpoint of the OWC entrance.

The RAO, as derived in [28] is given by Eqn. (9).

$$RAO(\omega) = \frac{\omega_0^2}{\sqrt{\left(\omega_0^2 - \omega^2\right)^2 + (2\zeta\omega\omega_0)^2}} \cdot \frac{\cosh\big(k(d - L_e)\big)}{\cosh(kd)} \tag{9}$$

The experimental RAO results were compared with the theoretical RAO in Equation (9) where ω_0^2 and ζ were found using the MATLAB `fittype` and `fit` functions.

Results comparing no air chamber and the 8 damping conditions (7 orifice diameters + Open device) are shown in Fig. 4. The larger wave condition (H_w = 40 mm) consistently produced a smaller peak in the RAO as a result of higher damping forces associated with viscous damping, radiation damping and dynamic air pressure.

Results comparing different auxiliary air chamber volumes are shown in Figs. 5, 6 and 7 for orifice diameters 25 mm, 35 mm, and 45 mm, respectively. It can be seen that larger air chambers resulted in higher peaks in the RAO, due to the flow of air mass through the connecting hose. This then leads to higher viscous losses and radiation damping. RAO results in Figs. 4 to 7

compare the experimental results (circles) and the linear fit (lines).

H. Phase

The average phase delay, ϕ, between the phase probe and the free surface excitation was calculated for each monochromatic wave period tested, by taking the time delay between the two wave probes averaged over the same number of waves used to calculate the RAO:

$$\phi° = \theta° - \frac{180}{\pi}\left(\tan^{-1}\frac{\omega_0^2 - \omega^2}{2\zeta\omega\omega_0}\right) \tag{10}$$

where θ is a correction applied as a result of the probe not being perfectly aligned with the 'centre' of oscillation of the device.

The MATLAB `fittype` and `fit` functions were used to first iteratively find θ and then ω_0 and ζ.

As can be seen in Fig. 4, the peak period occurs where the measured phase delay is = 65.8° (at the intersection point) instead of the expected 90°. This is due to the placement of the probe being parallel to the vertical section whereas the true 'centre' of the device, the location that would result in phase plots to intersect at 90°, is somewhere between the submerged entrance and the phase probe placement. This 'centre' location is situated at the front wall of the device which is also approximately where the chord line starts rising from horizontal.

I. Capture Width Ratio

The power 'output' of the device was characterised using the capture width ratio defined as

$$C_{WR} = \frac{P_{OWC}}{w_{OWC} \cdot P_w} \tag{11}$$

where P_{OWC} is the power through the orifice, w_{OWC} is the width of the device and P_w is the wave power per metre of wave front.

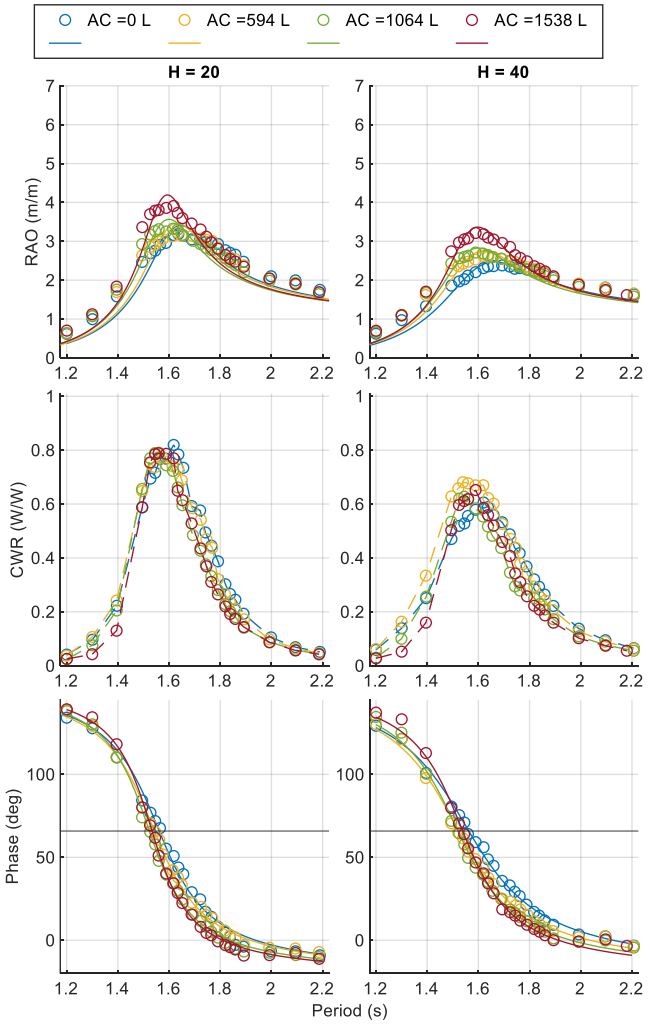

Fig. 6. Performance characteristic for single orifice diameter O = 35 mm added air chamber (AC = [0, 594, 1064, 1538] L). RAO (top) and Phase (bottom) results compare experimental results (circles) and the numerical fit (solid lines). CWR (middle) show experimental results only.

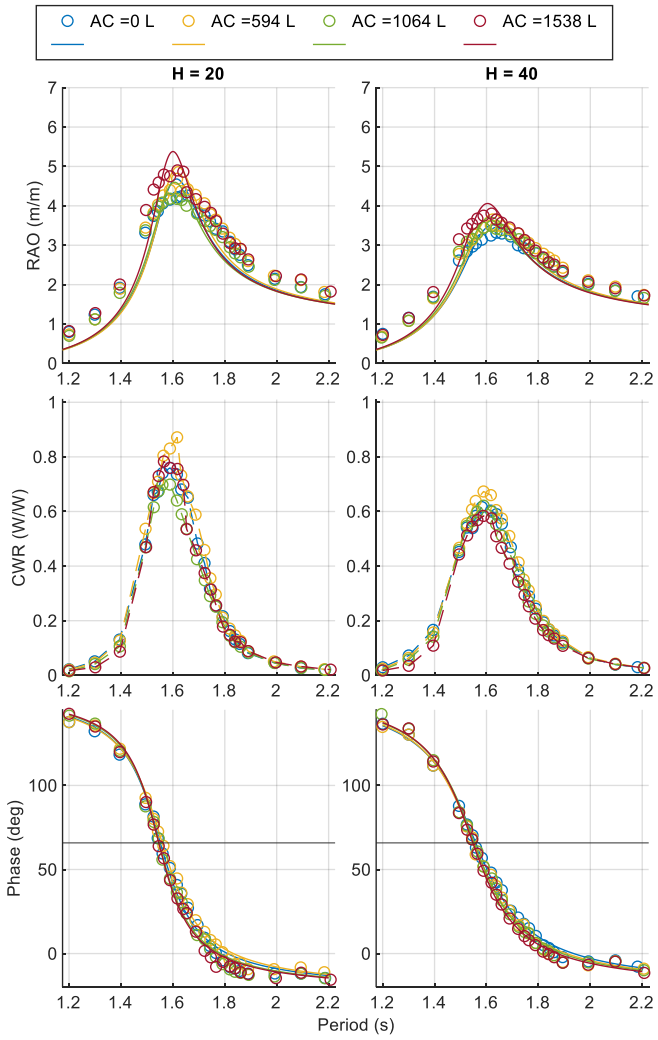

Fig. 7. Performance characteristic for single orifice diameter O = 45 mm added air chamber (AC = [0, 594, 1064, 1538] L). RAO (top) and Phase (bottom) results compare experimental results (circles) and the numerical fit (solid lines). CWR (middle) show experimental results only.

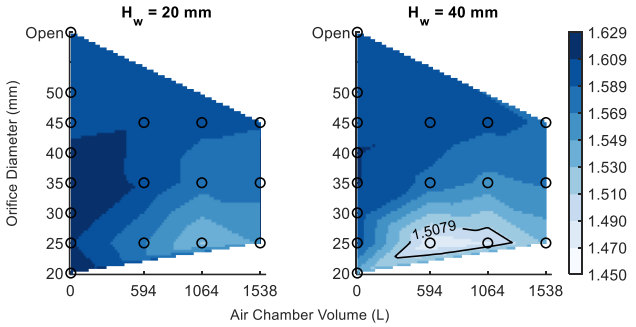

Fig. 8. Resonant period ($T_0 = \frac{2\pi}{\omega_0}$) results from curve fit on RAO. Contour in top right figure shows natural frequency, $T_n = 2\pi\sqrt{\frac{L_c}{g}}$

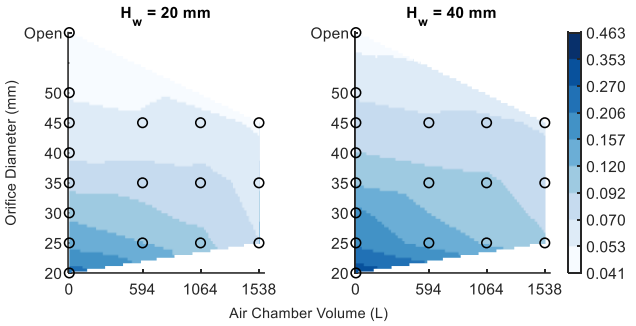

Fig. 10. Damping ratio (ζ) results curve fit on RAO. The colourbar values are on a logarithmic scale.

The wave power per metre is defined as [6]

$$P_w = \frac{1}{8}\rho_w g H_w^2 C_g \tag{12}$$

where ρ_w is the water density and C_g is the group velocity calculated as [6]

$$C_g = \frac{1}{2}\left(1 + \frac{2kd}{\sinh(2kd)}\right)\frac{\omega}{k} \tag{13}$$

The pneumatic power is defined as [6]

$$P_{OWC} = \frac{1}{t_{max}}\int_0^{t_{max}} p(t)Q_p(t)dt \tag{14}$$

where $p(t)$ is the pressure drop across the orifice and $Q_p(t)$ is the volumetric flow through the orifice. As

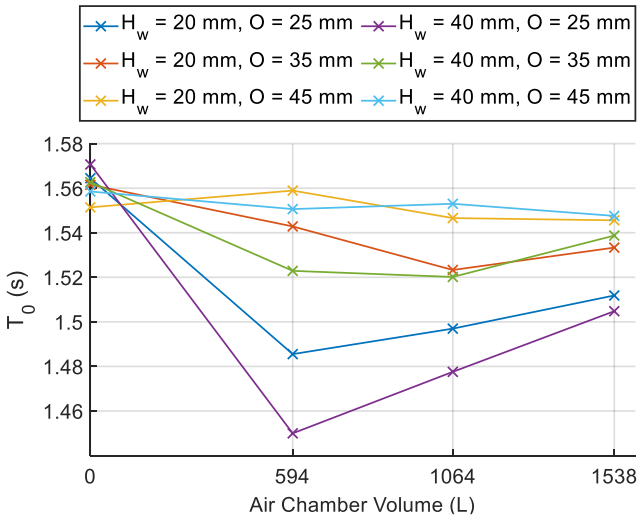

Fig. 12. T_0 (from phase) vs Air Chamber Volume

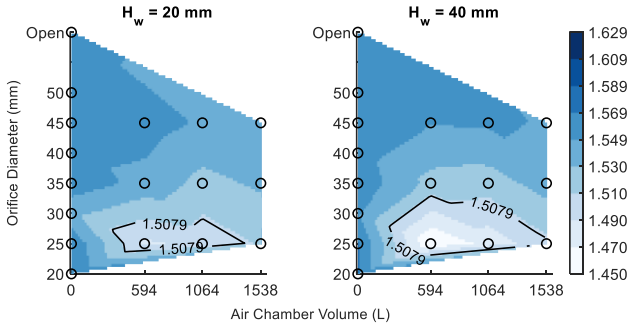

Fig. 9. Resonant period ($T_0 = \frac{2\pi}{\omega_0}$) results from curve fit on phase response. Contour line shows natural frequency, $T_n = 2\pi\sqrt{\frac{L_c}{g}}$

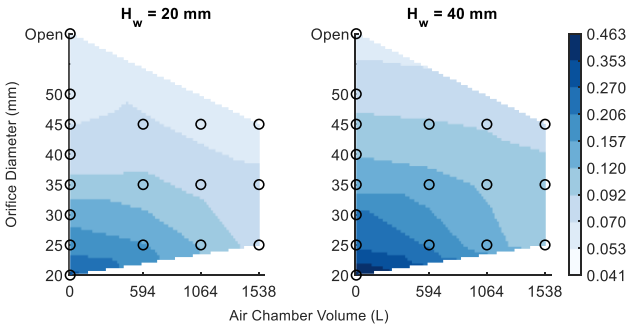

Fig. 11. Damping ratio (ζ) results from curve fit on phase response. The colourbar values are on a logarithmic scale.

shown in [21], the simplified expression of the flow rate through the orifice is sufficient to estimate pneumatic power and is as follows.

$$Q_p(t) = -\frac{dV}{dt} - \frac{V_0}{\gamma p_0}\frac{dp(t)}{dt} \tag{15}$$

where $\frac{dV}{dt}$ is the volume change of the air in the device due to the free surface excitation, V_0 is the still water air volume, $\gamma = 1.4$ is the specific heat ratio of the air and p_0 is atmospheric pressure.

Due to the recording artifact as mentioned in section II-D in the pressure sensor, the magnitude of the CWR peak should only be used for comparison purposes. Nonetheless, the peak location was found to match the resonant period of the RAO and phase analysis which do not use pressure sensor data. The CWR plots also exhibit the equal compression critical point described in [4]. From Fig. 4 is can be seen that the peak power 'output' occurs when the orifice diameter is $O = 40$ mm. While the RAO results show that a larger air chamber leads to a higher peak in response, this is not always seen in the CWR results as the air volume associated with peak power 'output' changes depending on the incident wave height and orifice.

J. Performance Characteristics Discussion

The main objective of this study was to characterize the device in part by determining resonant period (T_0) and damping ratio (ζ). As per sections III-G and III-H this was achieved via a MATLAB curve-fitting function applied to the RAO and Phase Response data. The results of this curve-fitting are presented in Figs. 8 to 11, which show an

interpolated colourmap of the resulting fit for all runs conducted. Comparing T_0 results for RAO (Fig. 8) to Phase Response (Fig. 9) the RAO fit was observed to consistently produce a higher T_0 (3% on average). Similarly the damping ratio curve fitting for the RAO (Fig. 10) was observed to produce consistently lower ζ (19% on average) than for the Phase Response (Fig. 11). These differences can be attributed to:

1. The phase wave data is not subject to as many sources of error as for RAO as precise wave height data is not required to measure the phase.
2. As peak resonance always occurs at $\phi = 90°$, T_0 is less affected by the linear approximation on the phase response as on the RAO.
3. The curve-fitting approximations overestimate the peak height in the RAO data and thus underestimates ζ.

Despite these diffferences both T_0 and ζ follow the same trends where ζ increases with decreasing orfice diameters and decreasing air volumes. T_0 exhibits an

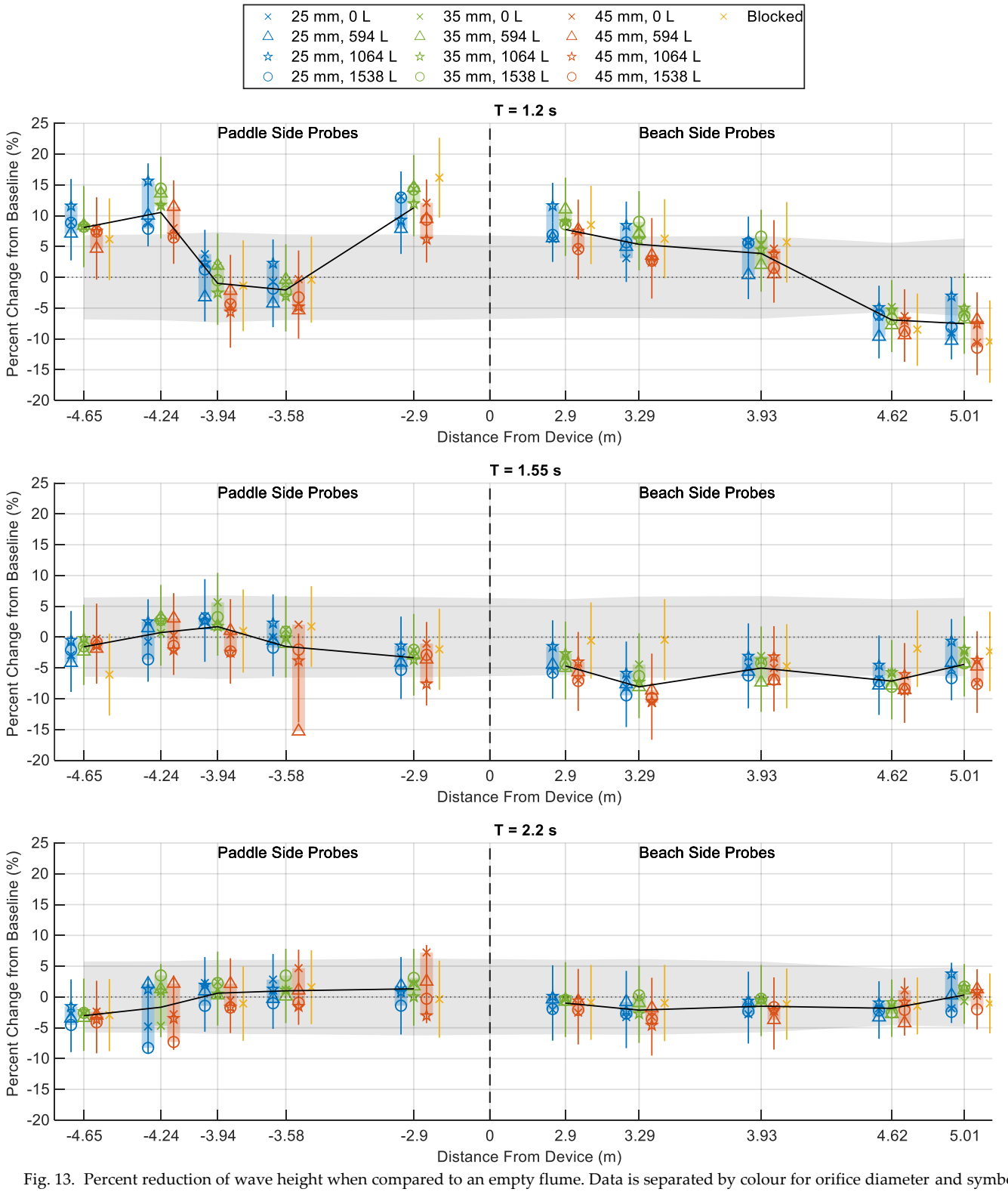

Fig. 13. Percent reduction of wave height when compared to an empty flume. Data is separated by colour for orifice diameter and symbol for air chamber volume. Periods represent the shortest, resonant, and longest periods. Grey areas are within the error margins of the probes. Vertical bars show the error margin between the air chamber tests. The black line shows the mean for all runs (excl. Blocked).

unexpected behaviour as air volumes increase.

Intuitively, increasing the air volume should lead to a decrease in the air-spring stiffness as more air is 'available' for compression thus increasing the resonant period. However, the opposite effect was observed here for every configuration, most notably at the highest damping (O = 25 mm) and varying the air chamber volume. This can be seen in Fig. 12, where the intermediate air chamber volumes resulted in the lowest resonant period.

Critically, this reduction in T_0 cannot be caused by a change in added mass (M_a) as the resonant period ($T_0 = 2\pi\sqrt{\frac{\rho_w A_w L_c + M_a}{\rho_w A_w g}}$) can only be less than the natural period ($T_n = 2\pi\sqrt{\frac{L_c}{g}}$) if a stiffness term is added to the denominator. Figs. 9 and 10 show the regions which $T_0 < T_n$ with a contour line at T_n. As a result, this method alone is limited for the purpose of assessing M_a.

K. Wave Height Reduction in the Lee of the OWC

For each test run, wave heights along the flume on both sides of the OWC were recorded at 15 separate locations shown in Fig. 1. A test without the device in the flume was also conducted for comparison. An additional test with the submerged entrance blocked was used to compare the active radiation effects of the OWC to its passive reflective properties.

The percentage change in wave height was calculated at each probe location for every run. This analysis is presented for three different incident wave periods in Fig. 13. The periods selected are the shortest and longest periods tested, as well as the resonant period. Note that as the wave probes are accurate within ±1 mm, most of the measured data points were within the error range of the probes themselves, and as such tests with a H_w = 20 mm are not considered for this analysis. The grey areas in Fig. 13 represent the region where the results fall withing the error range of the wave probes.

Given the 10% blockage ratio of the single OWC across the 3 m flume and 52% within the water column, a limited effect on the reflected and transmitted wave field is to be expected. Additionally, the OWC width to wavelength ratio is below 0.1 for all periods tested. Nonetheless, some interesting and consistent trends were observed:

1. The OWC in its active mode (i.e. not blocked) exhibits wave height reduction in the lee (beach side) of the device for periods close to resonance. This is not seen in the passive mode. This indicates that the energy absorbed by the OWC, and the resulting radiated waves have a marked effect close to resonance.
2. At periods away from resonance, there is little difference between the active and passive OWC.
3. The OWC exhibits a reflective regime during short period waves, and wave height reduction is more marked in the far field. A clear node from the reflected wave can be seen at T = 1.2 s in the offshore (paddle side) probes. This is seen in both active and passive modes.
4. The device has little effect on the wave height of longer periods.
5. Varying both the air chamber and orifice diameter did not produce a significant measurable change in the resulting wave heights both upstream and downstream of the device. This is shown in Fig. 13 by the vertical error bars showing the error margins of the probes.

Whilst the air compressibility scaling effects can have significant changes on the device performance characteristics, the results of this study suggest that the effects on the wave field are less significant.

While these small effects could be amplified when considering array interactions, the magnitude of the error which they present are small but must be considered. Based on the extensive flume testing results presented here, it is concluded that in future wave basin testing of various multi-device array configurations, it is acceptable to exclude the use of external air chambers to model individual device air volume.

ACKNOWLEDGEMENT

N. Cohen is funded by an Australian Government Research Training Program Scholarship at UNSW, with additional scholarship and research funding by Australian Research Council Linkage Project LP180101109.

REFERENCES

[1] D. Clemente, P. Rosa-Santos, and F. Taveira-Pinto, "On the potential synergies and applications of wave energy converters: A review," vol. 135, ed: Elsevier Ltd, 2021, pp. 110162-110162.

[2] IEA-OES, "Annual Report: An Overview of Ocean Energy Activities in 2022," 2023.

[3] J. Kirkegaard *et al.*, *Users Guide to Physical Modelling and Experimentation: Experience of the HYDRALAB Network*. 2011.

[4] J. C. C. Portillo, J. C. C. Henriques, L. M. C. Gato, and A. F. O. Falcão, "Model tests on a floating coaxial-duct OWC wave energy converter with focus on the spring-like air compressibility effect," *Energy,* vol. 263, pp. 125549-125549, 2023.

[5] J. Orphin, J.-R. Nader, and I. Penesis, "Size matters: Scale effects of an OWC wave energy converter," *Renewable Energy,* vol. 185, pp. 111-122, 2021.

[6] I. López, R. Carballo, D. M. Fouz, and G. Iglesias, "Design selection and geometry in OWC wave energy converters for performance," *Energies,* vol. 14, no. 6, pp. 1707-1707, 2021.

[7] I. López, R. Carballo, F. Taveira-Pinto, and G. Iglesias, "Sensitivity of OWC performance to air compressibility," *Renewable Energy,* vol. 145, pp. 1334-1347, 2020.

[8] A. Viviano, S. Naty, and E. Foti, "Scale effects in physical modelling of a generalized OWC," *Ocean Engineering,* vol. 162, no. April, pp. 248-258, 2018.

[9] D. Howe, J.-R. Nader, and G. Macfarlane, "Experimental analysis into the effects of air compressibility in OWC

model testing," *Proceedings of the 4th Asian Wave and Tidal Energy Conference,* no. September, 2018.

[10] F. Mahnamfar and A. Altunkaynak, "Comparison of numerical and experimental analyses for optimizing the geometry of OWC systems," *Ocean Engineering,* vol. 130, pp. 10-24, 2017.

[11] D. Howe, J. Orphin, J. Nader, and G. MacFarlane, "The effect of lip extrusion on performance of a breakwater integrated bent duct OWC WEC," *Proceedings of the 12th European Wave and Tidal Energy Conference. Cork, Ireland,* no. August, 2017.

[12] A. Elhanafi, G. Macfarlane, A. Fleming, and Z. Leong, "Scaling and air compressibility effects on a three-dimensional offshore stationary OWC wave energy converter," *Applied Energy,* vol. 189, pp. 1-20, 2017.

[13] B. Bosma, T. Brekken, P. Lomonaco, A. McKee, B. Paasch, and B. Batten, "Physical model testing and system identification of a cylindrical OWC device," in *Proceedings of the 12th European Wave and Tidal Energy Conference. Cork, Ireland*, 2017.

[14] I. López, A. Castro, and G. Iglesias, "Hydrodynamic performance of an oscillating water column wave energy converter by means of particle imaging velocimetry," *Energy,* vol. 83, pp. 89-103, 2015.

[15] I. López, B. Pereiras, F. Castro, and G. Iglesias, "Optimisation of turbine-induced damping for an OWC wave energy converter using a RANS–VOF numerical model," *Applied Energy,* vol. 127, pp. 105-114, 2014.

[16] A. Fleming, I. Penesis, G. MacFarlane, N. Bose, and T. Denniss, "Energy balance analysis for an oscillating water column wave energy converter," *Ocean Engineering,* vol. 54, pp. 26-33, 2012.

[17] A. F. O. Falcão and J. C. C. Henriques, "Model-prototype similarity of oscillating-water-column wave energy converters," *International Journal of Marine Energy,* vol. 6, pp. 18-34, 2014.

[18] P. Benreguig, M. Vicente, A. Dunne, and J. Murphy, "Modelling approaches of a closed-circuit OWC Wave energy converter," *Journal of Marine Science and Engineering,* vol. 7, no. 2, 2019.

[19] P. Rosa-Santos *et al.*, "Experimental study of a hybrid wave energy converter integrated in a harbor breakwater," *Journal of Marine Science and Engineering,* vol. 7, no. 2, pp. 1-18, 2019.

[20] W. Sheng and A. Lewis, "Wave energy conversion of oscillating water column devices including air compressibility," *Journal of Renewable and Sustainable Energy,* vol. 8, no. 5, 2016.

[21] W. Sheng, F. Thiebaut, M. Babuchon, J. Brooks, A. Lewis, and R. Alcorn, "Investigation to Air Compressibility of Oscillating Water Column Wave Energy Converters," 2013. Available: https://doi.org/10.1115/OMAE2013-10151

[22] A. Elhanafi, G. Macfarlane, A. Fleming, and Z. Leong, "Experimental and numerical measurements of wave forces on a 3D offshore stationary OWC wave energy converter," *Ocean Engineering,* vol. 144, pp. 98-117, 2017.

[23] A. Elhanafi, G. Macfarlane, A. Fleming, and Z. Leong, "Investigations on 3D effects and correlation between wave height and lip submergence of an offshore stationary OWC wave energy converter," *Applied Ocean Research,* vol. 64, pp. 203-216, 2017/03/01/ 2017.

[24] J. C. C. Portillo, L. M. C. Gato, J. C. C. Henriques, and A. F. O. Falcão, "Implications of spring-like air compressibility effects in floating coaxial-duct OWCs: Experimental and numerical investigation," *Renewable Energy,* vol. 212, pp. 478-491, 2023/08/01/ 2023.

[25] B. Bosma, T. Brekken, P. Lomonaco, B. Dupont, C. Sharp, and B. Batten, "Array modeling and testing of fixed OWC type wave energy converters," *International Marine Energy Journal,* vol. 3, no. 3, pp. 137-143, 2020.

[26] N. Y. Sergiienko, B. S. Cazzolato, N. Cohen, R. Manasseh, I. L. Turner, and F. Flocard, "The application of temporal gating in the measurement of response amplitude operators," presented at the Proceedings of the 15th European Wave and Tidal Energy Conference, Bilbao, Spain, 3-7 September, 2023.

[27] B. Bosma, Z. Zhang, T. K. A. Brekken, H. T. Özkan-Haller, C. McNatt, and S. C. Yim, "Wave energy converter modeling in the frequency domain: A design guide," in *2012 IEEE Energy Conversion Congress and Exposition (ECCE)*, 2012, pp. 2099-2106.

[28] D. Tothova, R. Manasseh, and S. A. Sannasiraj, "Identification of an initial non-linear transition in reciprocating finite-length pipe flow," *Physics of Fluids,* vol. 33, no. 12, p. 125111, 2021.

[29] I. Simonetti, L. Cappietti, H. El Safti, and H. Oumeraci, "Numerical modelling of fixed oscillating water column wave energy conversion devices: toward geometry hydraulic optimization," in *International Conference on Ocean, Offshore and Arctic Engineering*, 2015: American Society of Mechanical Engineers.

[30] J. Falnes and A. Kurniawan, *Ocean Waves and Oscillating Systems: Linear Interactions Including Wave-Energy Extraction*, 2 ed. (Cambridge Ocean Technology Series). Cambridge: Cambridge University Press, 2020.